

Thermally induced subgap features in the cotunneling spectroscopy of a carbon nanotube

S Ratz¹, A Donarini¹, D Steininger², T Geiger², A Kumar², A K Hüttel²,
Ch Strunk² and M Grifoni¹

¹Institute for Theoretical Physics, University of Regensburg, 93040 Regensburg, Germany

²Institute for Experimental and Applied Physics, University of Regensburg, 93040 Regensburg, Germany

E-mail: sascha.ratz@ur.de

Received 20 August 2014, revised 16 October 2014

Accepted for publication 7 November 2014

Published 15 December 2014

New Journal of Physics **16** (2014) 123040

doi:[10.1088/1367-2630/16/12/123040](https://doi.org/10.1088/1367-2630/16/12/123040)

Abstract

We report on the nonlinear cotunneling spectroscopy of a carbon nanotube quantum dot coupled to Nb superconducting contacts. Our measurements show rich *subgap* features in the stability diagram which become more pronounced as the temperature is increased. Applying a transport theory based on the Liouville–von Neumann equation for the density matrix, we show that the transport properties can be attributed to processes involving sequential as well as elastic and inelastic cotunneling of quasiparticles thermally excited across the gap. In particular, we predict thermal replicas of the elastic and inelastic cotunneling peaks, in agreement with our experimental results.

Keywords: cotunneling, thermal quasiparticles, carbon nanotube, quantum dot, superconducting contacts

1. Introduction

Due to proximity effects, a hybrid device made of a superconductor coupled to a mesoscopic normal conductor makes it possible to study a wide range of quantum phenomena. In particular, in the Coulomb blockade (CB) regime these include supercurrent transport carried by Cooper pairs [1–6], coherent electron transport in terms of multiple Andreev reflections [7–10], and



Content from this work may be used under the terms of the [Creative Commons Attribution 3.0 licence](https://creativecommons.org/licenses/by/3.0/). Any further distribution of this work must maintain attribution to the author(s) and the title of the work, journal citation and DOI.

quasiparticle transport [5, 11–18]. Andreev reflections lead to subgap structures with steps at bias voltage $2\Delta/ne$ ($n \in \mathbb{N}^+$) in the current–voltage characteristics [8–11, 13, 19, 20], which are smeared out by increasing the temperature [10, 13]. In contrast, increasing the temperature favors quasiparticle transport, as it increases the probability of thermal activation of quasiparticles across the gap. The emergence of a zero-bias peak inside the Coulomb diamond by increasing the temperature [10, 13] was explained in terms of resonant tunneling [11] of thermal quasiparticles. Recently the additional possibility of observing transport features due to sequential tunneling of thermally excited quasiparticles was theoretically proposed in [17] and experimentally confirmed in [18]. Such processes lead to thermal resonance lines within the Coulomb blockade region, parallel to the Coulomb diamond edges. Cotunneling processes due to quasiparticles, however, have so far been reported only for bias voltages above the superconducting energy gap [14, 15]. In this work we present measurements in complete agreement with theoretical predictions regarding thermally excited quasiparticle transport in the cotunneling regime.

Cotunneling is a transport process in which the quantum dot (QD) is either excited (inelastic cotunneling) or kept in the same state as the initial state (elastic cotunneling) by means of events involving tunneling to an intermediate virtual state. Thus, for the inelastic case a bias threshold corresponding to the excitation energy is required to enable charge transfer [21]. In contrast with sequential tunneling processes, cotunneling at the lowest order is expected to be independent of the gate voltage.

We report on elastic and inelastic cotunneling spectroscopy on individual carbon nanotube (CNT) devices coupled to Nb superconducting leads. In the low-temperature limit, transport theory predicts for a CNT quantum dot superconductivity enhanced transport features at bias voltages $\pm 2\Delta/e$ and $\pm(2\Delta + \delta_m)/e$ due to elastic and inelastic cotunneling of quasiparticles, respectively [14]. Here $\{\delta_m\}$ is the set of excitation energies of the CNT from an N -particle ground state. With increasing temperature, we predict and observe the appearance of elastic and inelastic cotunneling features in the subgap region (i.e., for bias voltage amplitudes smaller than $2\Delta/e$) due to thermally excited quasiparticles. In particular, the emergence of a zero-bias peak, corresponding to the thermal replica of the elastic cotunneling resonance, is expected. Our theoretical predictions are in good quantitative agreement with our experimental findings.

Individual single wall carbon nanotubes were grown on a highly p-doped Si/SiO₂ substrate by chemical vapor deposition [22]. The substrate acting as a global back gate is used to tune the electron occupation of the CNT. The source and drain electrodes were patterned on an individual single wall carbon nanotube by standard electron beam lithography and lift-off techniques. Here we report on measurements of two distinct samples. For sample A, figure 1, electrodes made of 3 nm Pd and 45 nm sputtered Nb with a spacing between electrodes on the order of 300 nm were used (see figure 1(a)); for sample B, figure A1 in the appendix, a metalization of 3 nm Pd and 60 nm sputtered Nb with a contact spacing on the order of 430 nm was applied (see figure A1(a)). To perform four-point measurements and as a resistive on-chip element, each superconducting electrode was connected to two leads made of AuPd to damp oscillations at the plasma frequency of the Josephson junction [23, 24]. Low-temperature electrical transport measurements were performed inside a 3He/4He dilution refrigerator with a base temperature of 25 mK.

In both samples we observe regular CB diamonds over a large gate voltage range. Signatures of fourfold periodicity are observed in the measured gate range only for sample A. Figures 1(b) and A1(b) show the high-resolution measurements for the selected gate range for

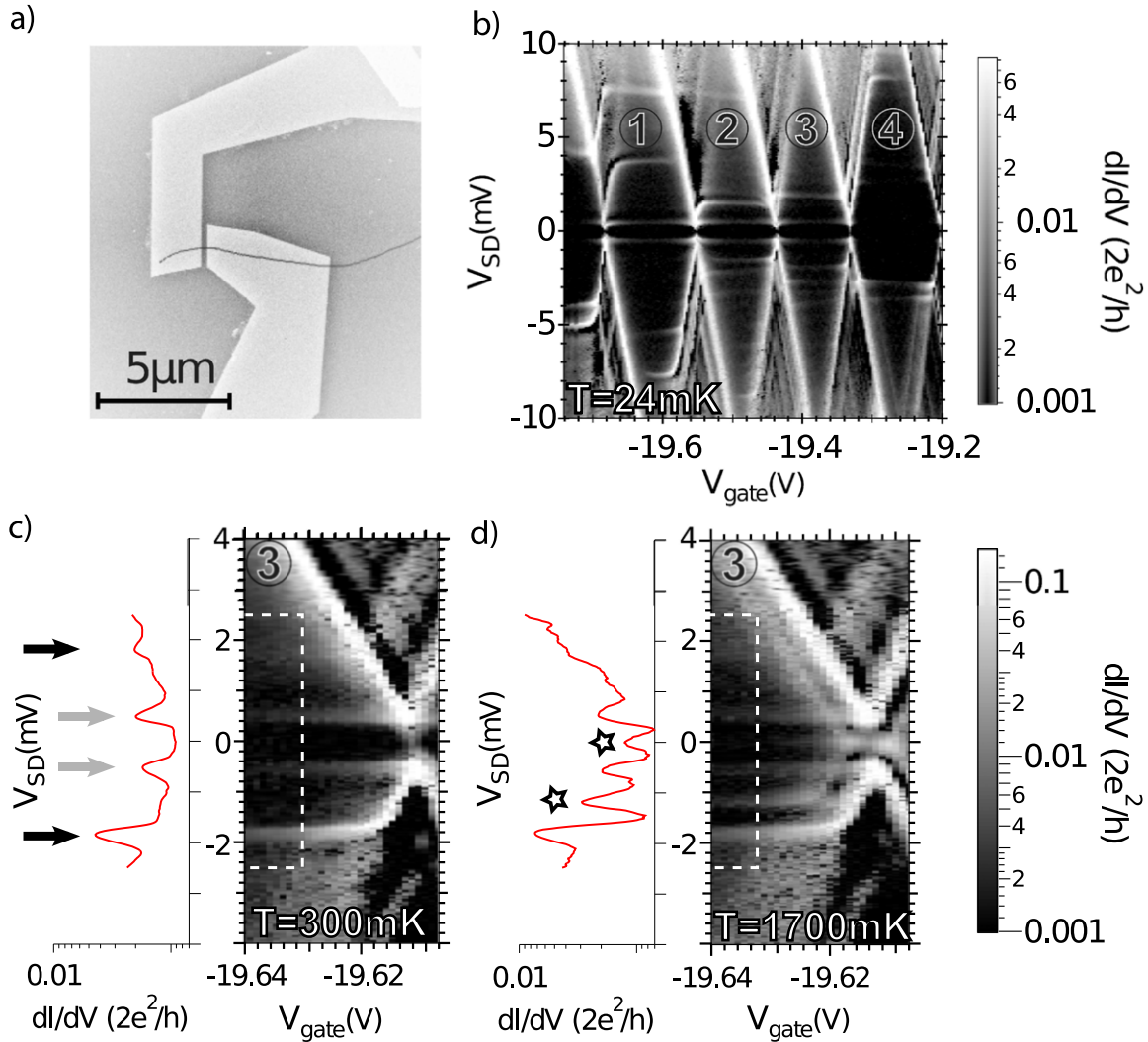


Figure 1. (a) Scanning electron micrograph of device A. The gray line indicates the approximated location of the nanotube (not visible itself). (b) Differential conductance at $T = 24$ mK as a function of bias voltage and back gate voltage. (c) (d) Zoom into the Coulomb blockade region of the third Coulomb diamond for temperatures $T = 300$ mK and $T = 1700$ mK, respectively. The dashed white box corresponds to the range of gate voltages that is averaged to obtain the differential conductance curve shown on the left side of each figure.

contacts in the superconducting state at temperature $T = 25$ mK and 30 mK, respectively. In both samples, lines of high conductivity are observed well inside the Coulomb diamonds; all these lines are horizontal, independent of gate voltage. To clearly identify them we restrict the gray scale for the differential conductance below the maximum conductance. Figure 1(c) shows a zoom corresponding to the region inside the diamond denoted ③ in figure 1(b)³. Horizontal lines are clearly visible and indicated by arrows in the conductance curve.

³ The discrepancy in gate voltage range between figures 1(b)–(d) is caused by a long-time scale drift of all Coulomb blockade features. Sequential tunneling features of this data set have already been discussed in [18].

One set of lines occurs at bias voltage $V_{SD} \sim \pm 0.52$ mV (gray arrows). We ascribe it to elastic cotunneling processes at $V_{SD} = \pm 2\Delta/e$. We extract $\Delta \sim 0.26$ meV for our superconducting film, compared with the expected value of $\Delta = 1.5$ meV for bulk Nb. The mismatch of about a factor of 5 has already been reported in similar Nb-based devices [14, 25–27]. The reason for the gap reduction is still an open question. Possible explanations are the formation of niobium oxide, the thin composite of Nb and Pd, or the contamination of the lower Nb interface. For the deposited Nb/Pd strip a critical temperature of about 8 K was measured, where the resonant features remain present up to temperatures of about 4–5 K. Thus the transition temperature of the thin film is comparable to bulk Nb, that is, in contrast with the observed small value of Δ and the BCS relation $\Delta = 1.76k_B T$. The inelastic part of the cotunneling spectra reveals excitations of the CNT quantum dot. Our data show a broad inelastic feature at a distance $\delta = 1.3$ meV from the elastic line (black arrows). From additional stability diagrams for sample A, recorded at higher temperature and finite magnetic field to suppress superconductivity, we extract a charging energy $E_C \simeq 15$ meV, implying $E_C/\Delta \sim 50$ for sample A. Similarly, from the elastic and inelastic line, we can also extract $\Delta \sim 0.23$ meV and $\delta \sim 0.11$ meV for sample B. From additional stability diagrams in a regime in which superconductivity is largely suppressed, we identify a smaller charging energy $E_C \simeq 3.2$ meV. The two samples have roughly the same superconducting gap Δ but differ in the charging energy E_C , leading to different transport regimes. In both samples charging effects and the small coupling strength $\hbar\Gamma < \Delta$ suppress Andreev processes, such that current is carried by quasiparticles. In sample A the large charging energy further suppresses multiple quasiparticle processes. Thus the transport is dominated by sequential and cotunneling events. For sample B a simple description in terms of resonant tunneling of quasiparticles [11] may be conceived.

As the temperature is increased, new horizontal lines are observed. In sample A the novel lines arise for temperatures above $T \approx 600$ mK at zero-bias and at bias voltage $V_{SD} = \pm \delta/e$. Figure 1(d) shows the same gate region as in figure 1(c) but now for the temperature $T = 1.7$ K. The additional lines, marked by stars, become more and more pronounced with increasing temperature. Andreev reflections do not give an explanation for the thermal behavior of such transition lines [4, 6–8, 27]. Also, the Kondo effect cannot be the reason for the resonant peak at zero bias, as it has an opposite thermal behavior [28–33].

The feature of a zero-bias conductance peak is also supported by sample B, as shown in figure A1(c) in appendix A. The bias trace is taken in the middle of the Coulomb blockade valley at gate voltage $V_{\text{gate}} \approx -11.71$ V. Upon increase of the temperature, one observes a rising conductance peak at zero bias and pairs of symmetrically displaced elastic and inelastic cotunneling peaks at finite bias. The feature at bias voltage $V_{SD} = \pm \Delta/e$ and the thermal zero-bias peak resemble data already reported in [10, 13]. In analogous fashion, we expect these to be reproducible within the simple resonant model of [11]. The more complex behavior of sample A, where several cotunneling and sequential lines are observed within the CB diamond, clearly goes beyond the capability of the simple resonant picture that excludes Coulomb interaction. As shown hereafter, a full transport theory that includes all tunneling processes up to the second order in the strength $\hbar\Gamma$ of coupling to the leads can capture the experimental behavior in great detail.

2. Transport theory for S-CNT-S junctions

To understand the experimental observations, we consider a minimal model for a CNT quantum dot connected to two BCS-type superconducting leads. For the back-gated CNT we consider a single longitudinal mode incorporating orbital, m , and spin, σ , degrees of freedom. Coulomb interaction effects are considered within a constant interaction model, with U being the charging energy. The quadruplet CNT Hamiltonian thus reads

$$\hat{H}_{\text{CNT}} = \sum_{m\sigma} E_{m\sigma} \hat{d}_{m\sigma}^\dagger \hat{d}_{m\sigma} + \frac{U}{2} \hat{N} (\hat{N} - 1) - \alpha e V_{\text{gate}} \hat{N}, \quad (1)$$

where \hat{N} is the charge number operator of the dot and α a conversion factor for the gate voltage. Finally, $E_{m\sigma} = \epsilon_d + \frac{1}{2} m \sigma \delta$ (with $m = \pm 1$, $\sigma = \pm 1$), where δ accounts for the breaking of the fourfold degeneracy of a longitudinal mode with energy ϵ_d due to spin-orbit interaction and valley mixing [34].

The BCS superconducting leads are described by a conventional pair-interaction Hamiltonian on a mean-field level with respect to an offset energy E_l^0 :

$$\hat{H}_l = E_l^0 + \sum_{\vec{k}\sigma} E_{l\vec{k}} \hat{\gamma}_{l\vec{k}\sigma}^\dagger \hat{\gamma}_{l\vec{k}\sigma} + \mu_l \hat{N}_l. \quad (2)$$

This can be obtained by means of a particle-conserving Bogoliubov–Valatin transformation [35, 36]:

$$\begin{aligned} \hat{c}_{l\vec{k}\sigma}^\dagger &= u_{l\vec{k}} \hat{\gamma}_{l\vec{k}\sigma}^\dagger + \sigma v_{l\vec{k}}^* \hat{S}_l^\dagger \hat{\gamma}_{l-\vec{k}\bar{\sigma}}, \\ \hat{c}_{l\vec{k}\sigma} &= u_{l\vec{k}}^* \hat{\gamma}_{l\vec{k}\sigma} + \sigma v_{l\vec{k}} \hat{S}_l \hat{\gamma}_{l-\vec{k}\bar{\sigma}}, \end{aligned} \quad (3)$$

for the leads' electron creation and annihilation operators $\hat{c}_{l\vec{k}\sigma}^\dagger$ and $\hat{c}_{l\vec{k}\sigma}$, respectively. The electron operators are represented in terms of quasiparticle operators $\hat{\gamma}_{l\vec{k}\sigma}^{(\dagger)}$ and of Cooper pair operators $\hat{S}_l^{(\dagger)}$ with the corresponding prefactors $u_{l\vec{k}}^{(*)}$ and $v_{l\vec{k}}^{(*)}$ [37, 38]. Furthermore, the quasiparticles have an excitation energy $E_{l\vec{k}} = \sqrt{(\epsilon_{\vec{k}} - \mu_l)^2 + \Delta^2}$ measured with respect to the electrochemical potential μ_l . Finally, the BCS gap is defined by,

$$\Delta \equiv |V| \sum_{\vec{k}} \left\langle \hat{S}_l^\dagger \hat{c}_{l-\vec{k}\downarrow} \hat{c}_{l\vec{k}\uparrow} \right\rangle \quad (4)$$

where $|V|$ characterizes the interaction potential between a pair of electrons.

The connection with the superconducting leads is achieved by a single-particle tunneling Hamiltonian $\hat{H}_{T,l} = T_l \sum_{\vec{k}\sigma m} \left(\hat{d}_{m\sigma}^\dagger \hat{c}_{l\vec{k}\sigma} + \text{h.c.} \right)$ where, for the sake of simplicity, the tunnel coefficient T_l of lead l is considered to be spin, wave vector, and valley independent. The tunnel coupling strength can then be defined as $\hbar \Gamma_l \equiv 2\pi |T_l|^2 \sum_{\vec{k}} \delta(\omega - \epsilon_{\vec{k}})$, which is assumed to be energy independent.

We describe the time evolution of the system with the generalized master equation [39]:

$$\dot{\hat{\rho}}_{\text{red}}(t) = -\frac{i}{\hbar} \left[\hat{H}_{\text{CNT}}, \hat{\rho}_{\text{red}}(t) \right] + \int_{t_0}^t d\tau \hat{K}(t, \tau) \hat{\rho}_{\text{red}}(\tau) \quad (5)$$

for the dynamics of the reduced density operator $\hat{\rho}_{\text{red}}$. This (still exact) equation allows a systematic perturbation expansion of the kernel superoperator $\hat{K}(t, \tau)$ in powers of the coupling strength $\hbar\Gamma$ [40, 41]. In the steady state limit and charge-conserved regime the master equation can be simplified further by applying the Laplace transform $f(\lambda) \equiv \int_0^\infty d\tau' e^{-\lambda\tau'} f(\tau')$ and its properties:

$$0 = -\frac{i}{\hbar} \sum_{\chi_i \chi_f} \delta_{\chi_i \chi_f} \delta_{\chi_i' \chi_f'} (E_{\chi_i} - E_{\chi_i'}) \rho_{\chi_i \chi_i'} + \sum_{\chi_i \chi_i'} K_{\chi_f \chi_f'}^{\chi_i \chi_i'} \rho_{\chi_i \chi_i'}, \quad (6)$$

with $K_{\chi_f \chi_f'}^{\chi_i \chi_i'} \equiv \langle \chi_f | \hat{K}(\lambda = 0^+) [|\chi_i\rangle \langle \chi_i'|] | \chi_f' \rangle$ and $\rho_{\chi_i \chi_i'} \equiv \langle \chi_i | \hat{\rho}_{\text{red}}(t \rightarrow \infty) | \chi_i' \rangle$. The matrix elements are evaluated in the basis $\{|\chi\rangle\}$ of the eigenstates of the Hamiltonian \hat{H}_{CNT} . Noticeably, each term in the perturbation expansion of $K_{\chi_f \chi_f'}^{\chi_i \chi_i'}$ can be represented in a diagrammatic language in which simple rules exist to directly obtain the corresponding analytical expression. In [42] these rules are derived and discussed in detail for the case of hybrid S–QD–S nanostructures.

An expression for the steady state current in terms of a perturbative expansion can be obtained in the same way. In particular, the net current of lead l is described by

$$I_l(t \rightarrow \infty) = e \sum_{\chi_f} \sum_{\chi_i \chi_i'} (K_{l_i})_{\chi_f \chi_f'}^{\chi_i \chi_i'} \rho_{\chi_i \chi_i'}. \quad (7)$$

In the charge-conserved regime the reduced density matrix $\rho_{\chi_i \chi_i'}$ is block diagonal (see appendix D). Thus the kernel element $K_{\chi_f \chi_f'}^{\chi_i \chi_i'}$ up to the second order also represents the physical rate for processes transferring 0, 1, or 2 charges, depending on the charge difference between the states $|\chi_i\rangle$ and $|\chi_f\rangle$.

The problem of non-equilibrium hybrid superconducting–quantum dot junctions with an applied bias voltage is intrinsically time dependent. This can lead to time-dependent harmonic contributions to the stationary current associated with Andreev tunneling [9]. However, in the charge-conserved regime considered in this work, these harmonics are absent, and hence $\hat{\rho}_{\text{red}}(t) \rightarrow 0$ at long times. This is because the expectation values $\langle \hat{c}_{l\bar{k}\sigma}^\dagger(t) \hat{c}_{l'\bar{k}'\sigma'}^\dagger(\tau) \rangle$ and $\langle \hat{c}_{l\bar{k}\sigma}(t) \hat{c}_{l'\bar{k}'\sigma'}(\tau) \rangle$ vanish since they break the conservation of total charge. Let us emphasize that, according to equation (4), we still have a finite superconducting gap and superconducting features (see appendix C for a detailed discussion).

Thermally assisted quasiparticle transport has up to now only been discussed in the context of sequential [17, 18] and resonant [10, 13] tunneling. Also responsible for the energy distribution of the fermionic quasiparticles, in addition to the BCS density of states (DOS), is the Fermi function. For high enough temperatures the Fermi function is thermally smeared, in the sense that quasiparticles can also occupy the high-energy branch of the DOS and thus can contribute to an additional transport channel. In the sequential tunneling regime, this gives rise to thermal replicas of the sequential tunneling transitions displaced by $\pm 4\Delta/e$ in bias voltage (solid orange lines in figure 2(a)). When cotunneling processes are also taken into account, the number of expected thermal lines is greatly increased, as sketched in figure 2(a). In the figure we restrict ourselves to the exemplary Coulomb diamond denoted ③. Gate-dependent lines, induced by sequential processes, can be clearly distinguished from gate-independent cotunneling induced lines. Solid and dashed blue lines are transitions which are due to ‘standard’ sequential tunneling and cotunneling processes, respectively, i.e., contributions that

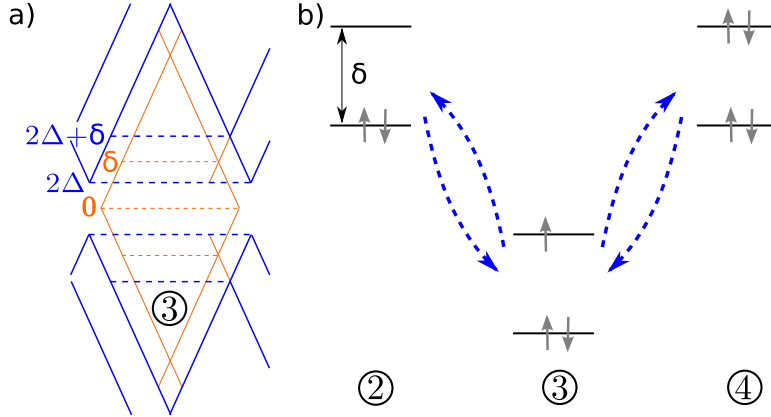


Figure 2. (a) Theoretically expected transition lines in the stability diagram of a CNT for a specific Coulomb diamond. Solid and dashed blue lines correspond to standard sequential tunneling and cotunneling processes, respectively. The thermal replicas of these transition lines are shown as solid and dashed orange lines. (b) Many-body spectrum of the 2-, 3- and 4-electron subspace for a gate voltage corresponding to center of the Coulomb diamond ③. The tunneling events contributing to the elastic cotunneling lines are shown.

are also present at low temperatures. Solid and dashed orange lines, in contrast, are due to thermally excited quasiparticles. Hence, they are present only at sufficiently high temperatures.

As already mentioned, standard elastic cotunneling lines are expected at bias $V_{SD} = \pm 2\Delta/e$, and the inelastic cotunneling features occur at a bias $V_{SD} = \pm(2\Delta + \delta)/e$, reflecting the excitation energy δ . Figure 2(b) visualizes the elastic cotunneling events in the many-body spectrum where the three-particle ground state is used as the reference energy. Choosing the center of diamond ③, corresponding to a certain gate voltage, the two-particle and four-particle ground states have the same energy. Thus, transitions from the three-particle ground state to the two-particle ground state and vice versa have the same probability as those from the three-particle ground state to the four-particle ground state and vice versa, leading to elastic cotunneling. As shown following, thermal excitation of the lead quasiparticles yields thermal replicas at a bias $2\Delta/e$, smaller than for standard cotunneling features. We thus predict, in particular, the emergence of a cotunneling line at zero bias, being the thermal replica of the standard elastic lines at $\pm 2\Delta/e$.

An exemplary contribution to elastic cotunneling in the diagrammatic language is shown in figure 3(a). Using the diagrammatic rules [41, 42], the analytic expression is given by the kernel element

$$\begin{aligned}
 (\hat{K}_{EC})_{xx}^{xx} &\equiv -i\hbar\Gamma_S\Gamma_D \sum_{\nu} \int \frac{d\omega}{2\pi} \frac{d\omega'}{2\pi} D_S(\omega, \Delta) D_D(\omega', \Delta) \\
 &\times \frac{f_S(\omega)(1 - f_D(\omega'))}{(-\omega + \delta E + i0^+)(\omega' - \omega + i0^+)(\omega' - \delta E + i0^+)} \\
 &\equiv -\frac{i}{\hbar}\Gamma_S\Gamma_D \sum_{\nu} \int \frac{d\omega}{2\pi} \frac{d\omega'}{2\pi} I(\omega, \omega'), \tag{8}
 \end{aligned}$$

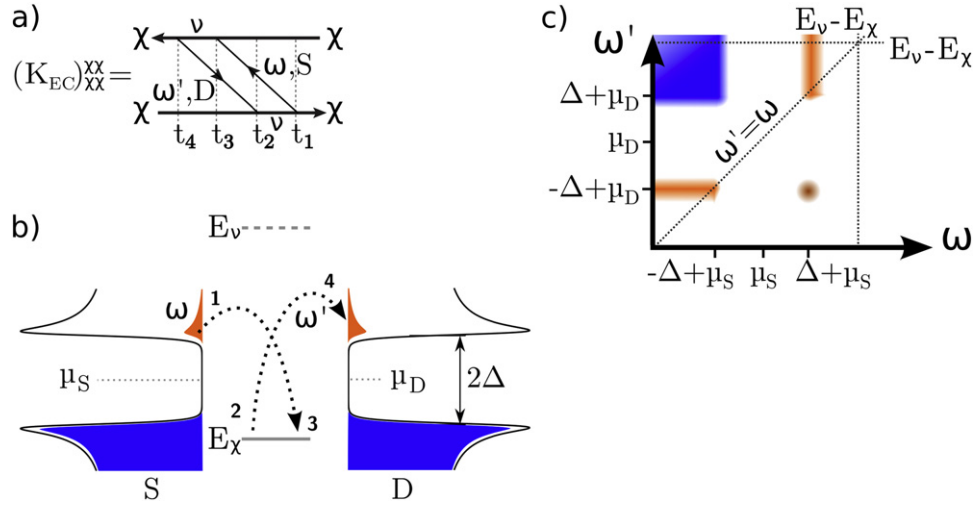


Figure 3. (a) Exemplary diagrammatic representation of a major contribution to elastic cotunneling. (b) Energy–DOS diagram explaining the transport mechanism for thermally assisted elastic cotunneling. The time ordering of the tunnel processes has the same declaration as in the diagram (a). A measurable elastic cotunneling current is observed if thermally occupied quasiparticle states in the source are simultaneously aligned with empty quasiparticle states in the drain. (c) Integrand of equation (8) for the parameter regime of figure (b). Blue corresponds to the low-temperature parameter regime $T \ll \Delta/k_B$, where the product of Fermi functions and density of states is finite. Orange represents the area where the product has to take higher temperatures $T < \Delta/k_B$ into account.

including $f_l(\omega) \equiv 1/[\exp((\omega - \mu_l)/k_B T) + 1]$, the DOS $D_l(\omega, \Delta) \equiv \sqrt{\frac{(\omega - \mu_l)^2}{(\omega - \mu_l)^2 - \Delta^2}} \times \Theta(|\omega - \mu_l| - \Delta)$, and the energy difference $\delta E = E_\nu - E_\chi$ between the energy E_ν of the virtual dot state $|\nu\rangle$ and E_χ of the dot state $|\chi\rangle$. Notice that in the example of figure 3(a), the state $|\nu\rangle$ has one unit of charge more than state $|\chi\rangle$. The charges entering and leaving the dot carry the energies ω and ω' , respectively. An analysis of the double integral shows that, at low temperatures, it gives a pronounced contribution only in the case $V_{SD} \geq 2\Delta/e$ (see appendix E). The bias threshold $V_{SD} = 2\Delta/e$ corresponds to the resonant case in which the highest occupied quasiparticle states in the source are aligned with the lowest empty quasiparticle states in the drain, such that elastic cotunneling onto and out of the CNT is possible. However, at higher temperatures thermally excited quasiparticles enable cotunneling transport also at zero bias. This mechanism is visualized in figure 3(b), where the numbers 1, 2, 3, 4 correspond to the tunneling events occurring at times $\tau \equiv t_1 \leq t_2 \leq t_3 \leq t_4 \equiv t$ shown in figure 3(a). As seen in figure 3(b), if the thermally occupied quasiparticle states of the source are in resonance with the unoccupied quasiparticle states of the drain, elastic cotunneling through the dot can also occur at zero bias. The tunneling rate $\Gamma_{EC}^{\chi \rightarrow \chi} \equiv 2 \text{Re}(\hat{K}_{EC})_{\chi\chi}^{\chi\chi}$ for such a process is given by the expression in equation (8), adding the hermitian conjugated.

Mathematically, the condition for the onset of elastic cotunneling can be obtained from the analysis of the integrand $I(\omega, \omega')$ of equation (8). This integrand is schematically depicted in figure 3(c) for the case of zero bias and $\Delta + \mu_{S/D} \ll \delta E$, such that the system is in the Coulomb blockade regime and no sequential transport occurs. Due to the product $D_S D_D f_S (1 - f_D)$, the

integrand $I(\omega, \omega')$ in equation (8) is non-vanishing at only low temperatures in the blue region of the $\omega - \omega'$ plane, depicted in figure 3(c). Upon increasing the temperature, the product is also non-vanishing along the orange stripes and on the orange spot.

In figure 3(c) the roots of the denominators are represented by dashed lines. It is evident that the integral of \hat{K}_{EC} has a large magnitude only in the case where the root line $\omega = \omega'$ and the colored regions meet when varying the bias voltage. Thus at low temperatures and $V_{SD} = 0$ no transport is possible because the corner of the blue region and the $\omega = \omega'$ line cannot touch. Upon increasing the temperature, transport is accessible through the orange regions at $\omega' = \mu_D - \Delta$ and $\omega = \mu_S - \Delta$; see the scheme in figure 3(c). This corresponds to the gate-independent resonance at zero bias. In this simple resonance picture, we obtain the elastic forward cotunneling rate (see appendix E) in the middle of a Coulomb diamond by a first approximation of the integrand in equation (8):

$$\Gamma_{\text{EC}}^{\chi \rightarrow \chi} = N_{\chi} \hbar \left(\frac{2}{U} \right)^2 \Gamma_S \Gamma_D \int \frac{d\omega}{2\pi} D(\omega, \Delta) D(\omega + eV_{SD}, \Delta) \times f(\omega) [1 - f(\omega + eV_{SD})], \quad (9)$$

where we directly pointed out the bias dependence of the rate and introduced a degeneracy factor N_{χ} depending on the state $|\chi\rangle$. Also including the backward process, the linear conductance is then approximated by

$$G = \left. \frac{dI}{dV_{SD}} \right|_{V_{SD}=0} \approx N_{\chi} \frac{e^2}{\hbar} \left(\frac{2}{U} \right)^2 \frac{\hbar^2 \Gamma_S \Gamma_D}{k_B T} \int \frac{d\omega}{2\pi} D^2(\omega, \Delta) f(\omega) f(-\omega). \quad (10)$$

This expression already shows a Boltzmann-like behavior $\exp[-\Delta/(k_B T)]$ for low temperatures $T \ll \Delta/k_B$ and reproduces the normal conducting result $G = N_{\chi} \frac{e^2}{h} \frac{\hbar^2 \Gamma_S \Gamma_D}{U^2}$ in the limit $\Delta \ll k_B T$. In particular, the former asymptotic characteristics indicate a transport property based on thermal excitation.

Analogously, subgap thermal replicas of the standard inelastic cotunneling lines are expected. We present a detailed analysis of the inelastic processes in appendix F and quote here the approximate result for the inelastic cotunneling rate:

$$\Gamma_{\text{EC}}^{\chi \rightarrow \chi'} = N_{\chi} \hbar \left(\frac{2}{U} \right)^2 \Gamma_S \Gamma_D \int \frac{d\omega}{2\pi} D(\omega, \Delta) D(\omega - \delta + eV_{SD}, \Delta) \times f(\omega) [1 - f(\omega - \delta + eV_{SD})], \quad (11)$$

similar to what was found in [14].

3. Comparison of theoretical and experimental predictions

In the following we use the BCS gap Δ , the excitation energy δ , and the charging energy E_C extracted from the measured differential conductance plots to calculate the current through the CNT by means of the generalized master equation. Since the measured data revealed a relatively large critical temperature, we can assume a temperature-independent gap size in the considered temperature regime $T < T_c/2$. The calculations are performed by approximating

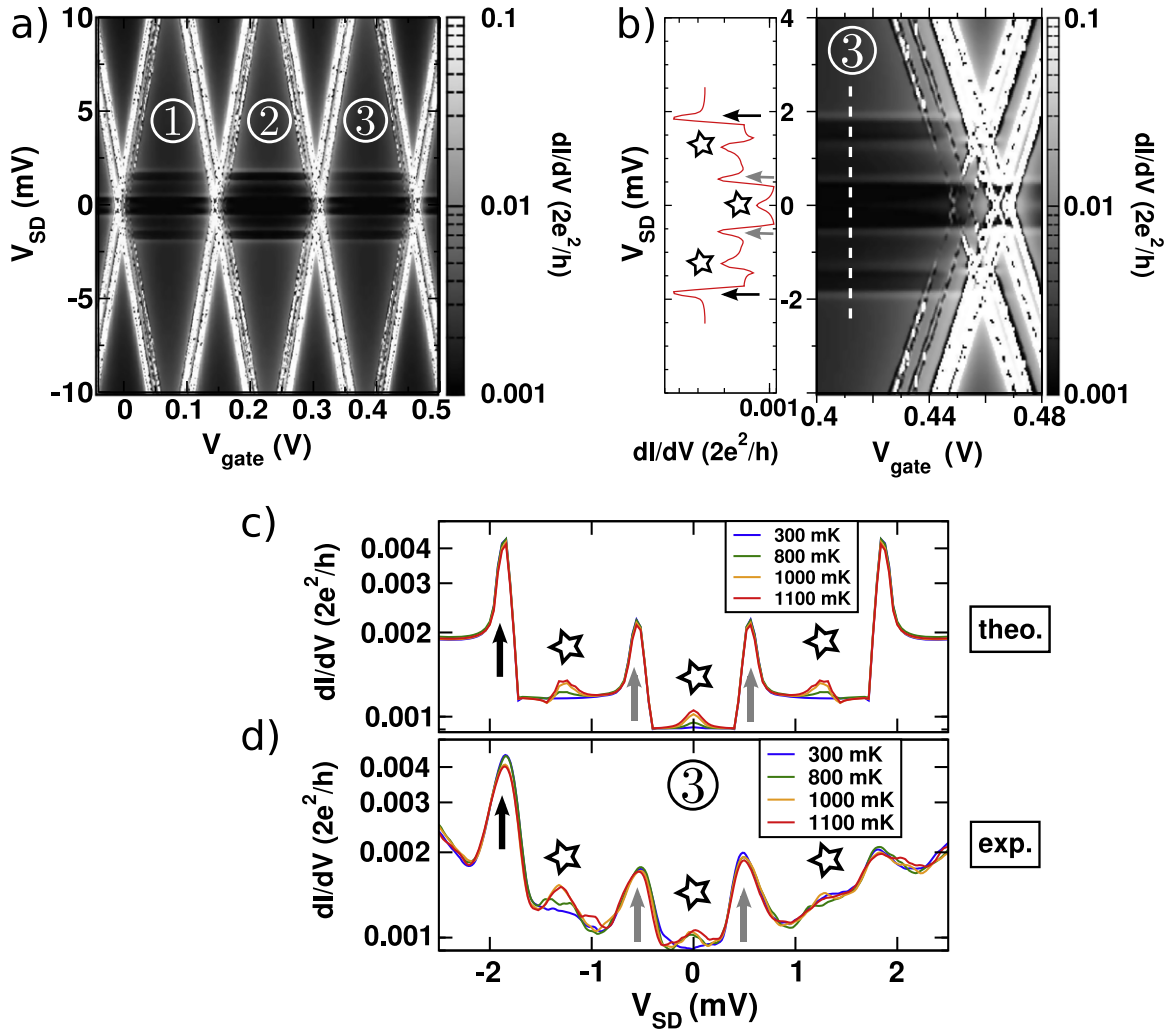


Figure 4. (a) Calculated differential conductance of a CNT with level splitting $\delta = 1.3$ meV and charging energy $E_C = 15$ meV. The temperature is $T = 1.7$ K and the BCS gap $\Delta = 0.26$ meV. The onset of inelastic and elastic cotunneling at $V_{SD} = \pm(2\Delta + \delta)/e$ and $V_{SD} = \pm 2\Delta$, respectively, yields horizontal transition lines. Also, gate-independent features at bias voltages $V_{SD} = \pm\delta/e$ and at zero bias can be pointed out. (b) Right panel: zoom into the right corner of diamond ③ indicated in (a). Left panel: bias trace corresponding to the gate voltage marked by the dashed white line in the right panel. In the bias trace the peaks indicated by stars are due to thermally activated quasiparticles. (c) Calculated bias traces for different temperatures. The peaks marked by stars correspond to thermal replicas of the standard cotunneling processes. To compare with the experiment we add a conductance offset of about $0.002 e^2/h$ to our numerical data. (d) Equivalent experimental data for comparison. The bias-dependent background results from the gradual increase of the conductance in the vicinity of the diamond edges.

the divergent DOS $D_l(\omega, \Delta)$ with a smoothened function.⁴ controlled by an empirical parameter γ similar to the Dynes parameter [43]. A good fit to the experimental data for sample A is obtained by $\gamma \approx 5.0 \mu\text{eV}$, a coupling strength $\hbar\Gamma = 0.01 \text{ meV}$, and a conversion factor $\alpha = 0.1$ for the gate voltage. The results of our transport calculations for sample A are shown in figures 4(a)–(c) for temperature $T = 1.7 \text{ K}$, such that $k_B T/\Delta = 0.56$. Figure 4(d) shows the corresponding experimental data for diamond ③. A short analysis of diamond ② is given in appendix B. In the bias and gate voltage range of figure 4(a) pronounced sequential tunneling lines and elastic and inelastic cotunneling features are seen. For better resolution we restrict the gray scale of the differential conductance below the maximum value. In figure 4(b) we focus on the Coulomb diamond denoted as ③. Beside the density plot we show the bias trace taken at the gate voltage marked by a white line, which supports the good quantitative agreement with the experimental data of figure 1(d). The standard cotunneling peaks (arrows) as well as their thermal replicas (stars) can be clearly recognized. The thermal behavior of the cotunneling features is illustrated in figures 4(c), (d), where the calculated and the measured differential conductance curves for different temperatures are presented. For the calculated curves we choose the same gate voltage as for the dashed white line in figure 4. For the experimental data we averaged a series of gate voltages marked by the box in figure 1(d). In both cases we emphasize that the standard cotunneling peaks are almost temperature independent, whereas the thermal replicas at zero bias and at $V_{SD} = \pm\delta/e$ rise with increasing temperature.

4. Conclusions

In summary, we report on new cotunneling transport properties of a CNT contacted with two superconducting Nb leads based on thermally assisted quasiparticle tunneling. We observe the thermal replica of the elastic and inelastic cotunneling resonances with increasing temperature above 600 mK. These lead to an extra zero-bias peak and to an inelastic peak corresponding to the lowest excitation energy in the dI/dV characteristics. To explain these non-equilibrium phenomena we derive a generalized master equation based on the RDM approach in the charge-conserved regime, applicable to any intradot interaction and finite superconducting gap. Modeling the CNT with a low-energy interacting spectrum, we find remarkable agreement with the experimental results concerning the thermal behavior of the additional cotunneling peaks.

Acknowledgments

The authors acknowledge fruitful discussions with C Chapelier. We gratefully acknowledge the support from the Deutsche Forschungsgemeinschaft (DFG) within GRK 1570, SFB 689, Emmy Noether (Hu 1808/1), and the EU FP7 Project SE2ND.

⁴ We replace the Heaviside function $\Theta(|\omega| - \Delta) \rightarrow \frac{1}{\exp(\gamma^{-1}(\omega + \Delta)) + 1} + \frac{1}{\exp(\gamma^{-1}(-\omega + \Delta)) + 1}$ by a blurred step function. Despite γ being introduced empirically in this work, it can be shown that higher order processes involving quasiparticles lead to level broadening in the quantum dot and thus also to regularization of the divergence caused by the BCS density of states [11] similar to that provided by γ here.

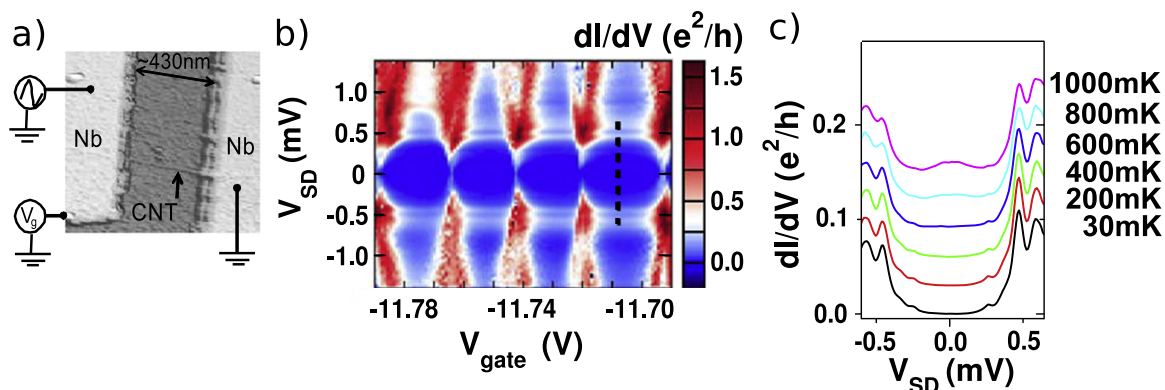


Figure A1. (a) Atomic force micrograph of device B. (b) Differential conductance at $T = 30$ mK as a function of bias voltage and back gate voltage. (c) Differential conductance curves in the low-bias regime for different temperatures at gate voltage $V_{\text{gate}} \approx -11.71$ V (dashed black line in b)). The bias trace shows a zero-bias peak emerging at increasing temperature. To see the feature more clearly a conductance offset of about $0.03 e^2/h$ was added systematically to each curve. The zero-bias peak is accompanied by the elastic and inelastic cotunneling peaks at negative and positive bias.

Appendix A. Experimental data of sample B

We have in addition confirmed the prediction of a zero-bias peak due to thermally excited elastic cotunneling in another experimental setup. The description of sample B can be found in the main text. An atomic force micrograph of the studied quantum dot device is shown in figure A1(a).

We observe regular Coulomb blockade diamonds over a large gate voltage range, also suggesting a defect-free CNT. In figure A1(b) we show high-resolution measurements for the selected gate range, including four Coulomb diamonds at temperature $T = 30$ mK. Inside the Coulomb diamonds we can identify gate-independent transition lines suggesting a symmetric coupling to the superconducting leads. To clarify the bias threshold of these horizontal lines, we take a bias trace of the region of interest at a fixed gate voltage $V_{\text{gate}} \approx -11.71$ V pointed out by the dashed line. This enables us to observe the onset of a stable conductance peak for temperatures above $T \approx 600$ mK which is more and more pronounced with increasing temperature. For that reason we assign the gate-independent conductance peak to a thermally assisted elastic cotunneling process. A detailed theoretical discussion follows in appendix D. However, a thermal replica of the inelastic cotunneling peak at bias voltage $V_{SD} = \pm 0.11$ meV cannot be clearly seen. This may be due to an overlap with the zero-bias peak.

Appendix B. Analysis of the Coulomb diamond ② of sample A

In figure B1 we show the bias trace of the measured differential conductance in the middle of the Coulomb diamond ② defined in the main text. It was obtained by the same averaging procedure as for the bias trace of diamond ③ explained in the main text. The curves for different temperatures include a richer peak structure than for the other diamond. We can identify the standard elastic cotunneling peaks at $V_{SD} = \pm 0.55$ mV as well as the inelastic peaks at $V_{SD} = \pm 2.2$ mV. The shift of the bias threshold for the excitation energy δ in comparison with

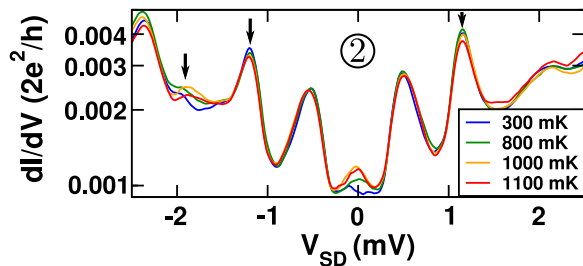


Figure B1. Measurement of the differential conductance of sample A taken in the middle of diamond ② for different temperatures. More features are observed than for diamond ③, indicating a more complex excitation structure of the CNT spectrum. We can see two additional excitation transition resonances, indicated by arrows, not observed in diamond ③.

the diamond ③ can be explained by a gate-dependent spin-orbit coupling in multielectron carbon nanotubes [44], as can also be seen in the overview figure 1(b). Besides, we can clearly recognize the rise of the thermal elastic cotunneling peak at zero bias with increasing temperature.

The additional features at bias voltage $V_{SD} = \pm 1.2$ mV cannot be explained by a single-shell model. Since the peak height is not temperature dependent, it must be a standard inelastic cotunneling feature. For our calculations we thus have to include a more complex excitation spectrum where the splitting to the next higher shell is smaller than δ . As was shown in [45], a two-particle ground state can lead to a rather complicated excitation spectrum where energetically close shells interact with each other, resulting in an effective shell splitting smaller than δ . Calculating such an effective Hamiltonian will remain a future task.

Also, the small peak at bias voltage $V_{SD} \approx -1.9$ mV is almost temperature independent. By inspection of the stability diagram, we classify it as a cotunneling assisted sequential tunneling process (COSET). In such a COSET an excited state is populated by a preceding inelastic cotunneling process yielding to a gate-dependent sequential resonance peak inside the Coulomb blockade regime [41, 46, 47]. A more detailed discussion is left for future work.

Appendix C. BCS theory in the charge-conserved regime

In macroscopic superconductors with a large number of particles, the boson-like condensate is well described by a phase coherent state $|\Phi\rangle$ with definite phase Φ . The presence of a relative phase between two weakly linked superconductors is at the origin of the Josephson effect [37, 48, 49]. In mesoscopic superconductors, charging effects due to Coulomb interaction break the degeneracy of states with a different number M of Cooper pairs. In such cases the phase Φ becomes uncertain and one has to project the state $|\Phi\rangle$ onto a state $|2M\rangle$ with a fixed Cooper pair number M [50, 51]. In this phase incoherent regime, the BCS Hamiltonian is thus properly diagonalized by means of the particle number-conserving Bogoliubov–Valatin transformation

$$\hat{c}_{\vec{k}\sigma}^\dagger = u_{\vec{k}} \hat{\gamma}_{\vec{k}\sigma}^\dagger + \sigma v_{\vec{k}}^* \hat{S}^\dagger \hat{\gamma}_{-\vec{k}\bar{\sigma}}, \quad (\text{C.1})$$

$$\hat{c}_{\vec{k}\sigma} = u_{\vec{k}} \hat{\gamma}_{\vec{k}\sigma} + \sigma v_{\vec{k}} \hat{S} \hat{\gamma}_{-\vec{k}\bar{\sigma}}^{\dagger}, \quad (\text{C.2})$$

including quasiparticle, $\hat{\gamma}_{\vec{k}\sigma}^{(\dagger)}$, as well as Cooper pair, $\hat{S}^{(\dagger)}$, operators. From the fermionic excitations described by the quasiparticle operators we demand $\{\hat{\gamma}_{\vec{k}\sigma}, \hat{\gamma}_{\vec{k}'\sigma'}^{\dagger}\} = \delta_{\vec{k}\vec{k}'} \delta_{\sigma\sigma'}$. Moreover, the Cooper pair condensate and the quasiparticles are decoupled, i.e.,

$$\left[\hat{S}^{(\dagger)}, \hat{\gamma}_{\vec{k}'\sigma'}^{(\dagger)} \right] = 0. \quad (\text{C.3})$$

By means of these commutator relations, we can further show that for the number operator \hat{N} of the electrons it holds that

$$\left[\hat{N}, \hat{S}^{\dagger} \right] = 2\hat{S}^{\dagger}, \quad (\text{C.4})$$

i.e., the Cooper pair operator keeps the system in a state with a well-defined charge number:

$$\hat{S} |2M\rangle = |2M - 2\rangle. \quad (\text{C.5})$$

Together with equation (C.3), we conclude that the Cooper pair condensate is the vacuum state for the quasiparticles and that fermionic excitations can be described by

$$\hat{\gamma}_{\vec{k}\sigma}^{\dagger} |0, 2M\rangle = |\vec{k}\sigma, 2M\rangle, \quad (\text{C.6})$$

$$\hat{\gamma}_{\vec{k}\sigma} |0, 2M\rangle = 0. \quad (\text{C.7})$$

In the phase incoherent regime, the equilibrium grand canonical density operator of the superconductor is given by

$$\hat{\rho}_R = \frac{e^{-\beta \hat{H}_{gc}}}{Z}, \quad (\text{C.8})$$

with $\beta^{-1} \equiv k_B T$ the inverse temperature. Here $Z \equiv \text{Tr}_R \left(e^{-\beta \hat{H}_{gc}} \right)$ is the partition function, where we introduced the grand canonical Hamiltonian $\hat{H}_{gc} \equiv \hat{H} - \mu \hat{N}$, and \hat{H} is as defined in equation (2) of the main text. Accounting for the properties in equations (C.5)–(C.7) of the quasiparticle and Cooper pair operators, the calculation of the thermal expectation value,

$$\begin{aligned} \langle \hat{O} \rangle &\equiv \text{Tr}_R (\hat{\rho}_R \hat{O}) \\ &= \sum_{\{n_{\vec{k}\sigma}\}, M} \langle \{n_{\vec{k}\sigma}\}, 2M | \hat{\rho}_R \hat{O} | \{n_{\vec{k}\sigma}\}, 2M \rangle, \end{aligned} \quad (\text{C.9})$$

of an operator \hat{O} in the basis $\{ | \{n_{\vec{k}\sigma}\}, 2M \rangle \}$ of the superconducting lead remains a standard task.

In the main text we claimed that the superconducting gap is not vanishing in the charge-conserved regime. The statement can be proved in the following way:

$$\begin{aligned}
\Delta &\equiv |V| \sum_{\vec{k}} \left\langle \hat{S}^\dagger \hat{c}_{-\vec{k}\downarrow} \hat{c}_{\vec{k}\uparrow} \right\rangle \\
&= |V| \sum_{\vec{k}} \text{Tr}_R \left(\hat{\rho}_R \hat{S}^\dagger \left(u_{-\vec{k}}^* u_{\vec{k}} \hat{\gamma}_{-\vec{k}\downarrow} \hat{\gamma}_{\vec{k}\uparrow} - v_{-\vec{k}} v_{\vec{k}} \hat{S} \hat{\gamma}_{\vec{k}\uparrow}^\dagger \hat{S} \hat{\gamma}_{-\vec{k}\downarrow}^\dagger - u_{\vec{k}}^* v_{-\vec{k}} \hat{S} \hat{\gamma}_{\vec{k}\uparrow}^\dagger \hat{\gamma}_{\vec{k}\uparrow} \right. \right. \\
&\quad \left. \left. + u_{-\vec{k}}^* v_{\vec{k}} \hat{\gamma}_{-\vec{k}\downarrow} \hat{S} \hat{\gamma}_{-\vec{k}\downarrow}^\dagger \right) \right) \\
&= |V| \sum_{\vec{k}} -u_{\vec{k}}^* v_{-\vec{k}} f(E_{\vec{k}}) + u_{-\vec{k}}^* v_{\vec{k}} (1 - f(E_{-\vec{k}})), \tag{C.10}
\end{aligned}$$

where in the last line we have used the orthogonality $\langle 2M | (\hat{S}^\dagger \hat{S}) | 2M \rangle = (1 - \delta_{M0})$ of the Cooper pair states, and $\langle \vec{k}\sigma | \vec{k}'\sigma' \rangle = \delta_{\vec{k}\vec{k}'} \delta_{\sigma\sigma'}$ of the quasiparticle states. Moreover, $\langle \hat{\gamma}_{\vec{k}\uparrow}^\dagger \hat{\gamma}_{\vec{k}\uparrow} \rangle = f(E_{\vec{k}})$, with $f(x) = 1/(e^x + 1)$. Indeed, the superconducting gap has a finite magnitude whose value depends on the temperature, as known from the BCS theory.

In the same manner it can be shown that the expectation values $\langle \hat{c}_{\vec{k}\sigma}^\dagger \hat{c}_{\vec{k}'\sigma'} \rangle$ and $\langle \hat{c}_{\vec{k}\sigma} \hat{c}_{\vec{k}'\sigma'} \rangle$ vanish in the charge-conserved regime.

Appendix D. Transport in the charge-conserved regime

For superconducting leads in the phase incoherent regime charge is conserved. This fact has important consequences when viewing quantum transport through a quantum dot coupled to such charge-conserved BCS leads. Because the tunneling Hamiltonian \hat{H}_T (equation (9) of the main text) and the quantum dot Hamiltonian are also charge conserving, charge is conserved during transport. As a consequence, the quantum dot density operator $\hat{\rho}_{red}$ is block diagonal in the charge representation. In other words, there are no coherences between states with different numbers of Cooper pairs. Let us emphasize that Cooper pairs still take part in tunneling events, as we will show in appendix E when analyzing a contribution to elastic cotunneling in terms of transport characteristics.

Appendix E. Analysis of the elastic cotunneling diagram

From a standard evaluation of the multiple commutators [41] constituting the kernel $\hat{K}(t, \tau)$, we obtain for the matrix element $(\hat{K}_{EC})_{\chi\chi}^{\chi\chi} \equiv \int_0^\infty dt' e^{-0^+t'} \langle \chi | \hat{K}(t, t-t') [|\chi\rangle\langle\chi|] | \chi \rangle$ the expression

$$\begin{aligned}
(\hat{K}_{EC})_{\chi\chi}^{\chi\chi} &= \sum_{\vec{k}\sigma, \vec{k}'\sigma'} \sum_{mm'\nu} \int_0^\infty dt' e^{-0^+t'} \int_0^{t'} dt_1' \int_0^{t_1'} dt_2' \left\langle \hat{c}_{S\vec{k}\sigma}^\dagger(\tau) \hat{c}_{S\vec{k}\sigma}(t_2) \right\rangle \\
&\quad \left\langle \hat{c}_{D\vec{k}'\sigma'}(t_1) \hat{c}_{D\vec{k}'\sigma'}^\dagger(t) \right\rangle \frac{|T_S|^2 |T_D|^2}{\hbar^4} \\
&\quad \times \left\langle \chi \left| \hat{d}_{m'\sigma'}(t) \right| \nu \right\rangle \left\langle \nu \left| \hat{d}_{m\sigma}^\dagger(t_2) \right| \chi \right\rangle \left\langle \chi \left| \hat{d}_{m\sigma}(\tau) \right| \nu \right\rangle \left\langle \nu \left| \hat{d}_{m'\sigma'}^\dagger(t_1) \right| \chi \right\rangle,
\end{aligned}$$

whose diagrammatic representation is shown in figure E1 (a). For the time differences we used the notation $t' \equiv t - \tau$, $t_1' \equiv t - t_1$ and $t_2' \equiv t - t_2$. When evaluating the expectation values of

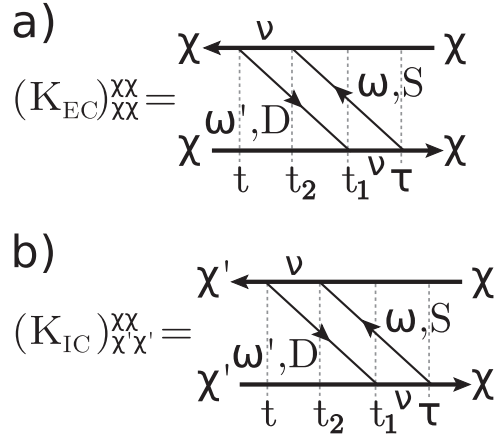


Figure E1. Diagrammatic representation of a relevant contribution to elastic (a) and inelastic (b) cotunneling. Necessary for the inelastic part is the energetic excitation of the final state χ' in comparison with the initial state χ , with both states having the same amount of charge.

the electron lead operators we need the Bogoliubov transform, equations (C.1) and (C.2). We then see also that Cooper pairs give contributions to the transport process through the acting operators $\hat{S}^{(\dagger)}$. We find:

$$\begin{aligned}
& \left\langle \hat{c}_{S\bar{k}\sigma}^\dagger(\tau) \hat{c}_{S\bar{k}\sigma}(t_2) \right\rangle \\
&= \left\langle \left(u_{S\bar{k}} \hat{\gamma}_{S\bar{k}\sigma}^\dagger(\tau) + \sigma v_{S\bar{k}}^* \hat{S}_S^\dagger(\tau) \hat{\gamma}_{S-\bar{k}\bar{\sigma}}(\tau) \right) \right. \\
&\quad \left. \times \left(u_{S\bar{k}}^* \hat{\gamma}_{S\bar{k}\sigma}(t_2) + \sigma v_{S\bar{k}} \hat{S}_S(t_2) \hat{\gamma}_{S-\bar{k}\bar{\sigma}}^\dagger(t_2) \right) \right\rangle \\
&= \left| u_{S\bar{k}} \right|^2 \exp \left[-\frac{i}{\hbar} (E_{S\bar{k}} + \mu_S)(t' - t_2') \right] \left\langle \hat{\gamma}_{S\bar{k}\sigma}^\dagger \hat{\gamma}_{S\bar{k}\sigma} \right\rangle \\
&\quad + \left| v_{S\bar{k}} \right|^2 \exp \left[\frac{i}{\hbar} (-E_{S\bar{k}} - \mu_S)(t' - t_2') \right] \left\langle \hat{S}_S^\dagger \hat{\gamma}_{S-\bar{k}\bar{\sigma}} \hat{S}_S \hat{\gamma}_{S-\bar{k}\bar{\sigma}}^\dagger \right\rangle \\
&= \left| u_{S\bar{k}} \right|^2 \exp \left[-\frac{i}{\hbar} (E_{S\bar{k}} + \mu_S)(t' - t_2') \right] \left[\exp(\beta E_{S\bar{k}}) + 1 \right]^{-1} \\
&\quad + \left| v_{S\bar{k}} \right|^2 \exp \left[-\frac{i}{\hbar} (E_{S\bar{k}} + \mu_S)(t' - t_2') \right] \left[\exp(\beta E_{S\bar{k}}) + 1 \right]^{-1} \\
&= \exp \left[-\frac{i}{\hbar} (E_{S\bar{k}} + \mu_S)(t' - t_2') \right] \left[\exp(\beta E_{S\bar{k}}) + 1 \right]^{-1},
\end{aligned}$$

where in the last line we used the normalization condition $|u_{\bar{k}}|^2 + |v_{\bar{k}}|^2 = 1$. The second expectation value can be calculated in a similar way such that for the kernel component of the elastic cotunneling we obtain

$$\begin{aligned}
(\hat{K}_{\text{EC}})_{\chi\chi}^{\chi\chi} &\equiv \sum_{\bar{k}\bar{k}'} \sum_{\nu} \int_0^{\infty} dt_2' \int_{t_2'}^{\infty} dt_1' \int_{t_1'}^{\infty} dt' e^{-0^+t'} \\
&\times \exp\left[-\frac{i}{\hbar}(E_{S\bar{k}} + \mu_S)(t' - t_2')\right] \exp\left[\frac{i}{\hbar}(E_{D\bar{k}'} + \mu_D)t_1'\right] \\
&\times \left(\exp[\beta E_{S\bar{k}}] + 1\right)^{-1} \left(\exp[-\beta E_{D\bar{k}'}] + 1\right)^{-1} \exp\left[\frac{i}{\hbar}(E_{\chi} - E_{\nu})t_2'\right] \\
&\times \exp\left[-\frac{i}{\hbar}(E_{\chi} - E_{\nu})(t' - t_1')\right] \frac{|T_S(\chi, \nu)|^2 |T_D(\chi, \nu)|^2}{\hbar^4} \\
&= -i\hbar\Gamma_S\Gamma_D \sum_{\nu} \int \frac{d\omega}{2\pi} \frac{d\omega'}{2\pi} D_S(\omega, \Delta) D_D(\omega', \Delta) \\
&\times \frac{f_S(\omega)(1 - f_D(\omega'))}{(-\omega + E_{\nu} - E_{\chi} + i0^+)(\omega' - \omega + i0^+)(\omega' + E_{\chi} - E_{\nu} + i0^+)} \\
&\equiv -i\hbar\Gamma_S\Gamma_D \sum_{\nu} \int \frac{d\omega}{2\pi} \frac{d\omega'}{2\pi} I(\omega, \omega'), \tag{E.1}
\end{aligned}$$

which is the same result as in the main text with $T_l(\chi, \nu) \equiv \sqrt{\tilde{\rho}_l} \sum_{m\sigma} T_l \langle \chi | \hat{d}_{m\sigma} | \nu \rangle$ and the electron density of states $\tilde{\rho}_l$ in lead l . In the last step the variable transformation $\tilde{t}_1 \equiv t_1' - t_2'$, $\tilde{t} \equiv t' - t_1'$ was applied in order to decouple the three time integrations. In addition, we expressed the energies ω, ω' with respect to the electrochemical potential μ_l .

To investigate the case when the double integral, and thus the kernel component, gives a relevant contribution to the transport dynamics, we analyze the integrand in detail. We are mainly interested in the region in the bias and gate voltage range in which the system is blocked into the ground state of the corresponding Coulomb blockade region in the sense of the sequential tunneling limit. If N electrons are trapped in the N -Coulomb diamond, the condition for a strong Coulomb blockade is $\mu_{S/D} - \Delta \ll E_{N\pm 1} - E_N$. In our example the ground state energy for N charges is E_{χ} , whereas E_{ν} is the energy of the $(N + 1)$ -particle state $|\nu\rangle$. Hence, in the blockade regime is $\mu_{S/D} - \Delta \ll E_{\nu} - E_{\chi}$. Moreover, taking the product of the Fermi function and the BCS density of states (figure E2 (a)) into account, only the blue region of the $\omega - \omega'$ plane, depicted in figure E2(b), is relevant for the integrand $I(\omega, \omega')$ in equation (E.1) at low temperatures. Upon increasing the temperature, the product of Fermi functions and BCS density of states in the integrand $I(\omega, \omega')$ is also non-vanishing along the orange stripes (figures E3 (a) and (b)).

The colored regions in the figure are the relevant energy region where the product of the density of states and the Fermi functions $D_S D_D f_S (1 - f_D) \gg 0$ is not vanishing.

In figures E2(b) and E3(b) the roots of the denominators are represented by dashed lines. As explained in the main text, we are looking for the cases in which the roots meet the colored regions. In particular, the threshold for the onset of standard elastic cotunneling processes is obtained for those values of the bias voltage such that the $\omega = \omega'$ root touches the corner of the blue region (see figure E2(b)). In that case the blue region includes the horizontal and the diagonal ($\omega' = \omega$) zeros of the denominators. Thus the bias threshold $V_{SD} = \pm 2\Delta/e$ for the low-temperature regime is obtained when the condition $\Delta + \mu_D = \omega' = \omega = -\Delta + \mu_S$ is used together with $\mu_S - \mu_D = eV_{SD}$. Note that for this bias voltage the diagonal zeros are located at

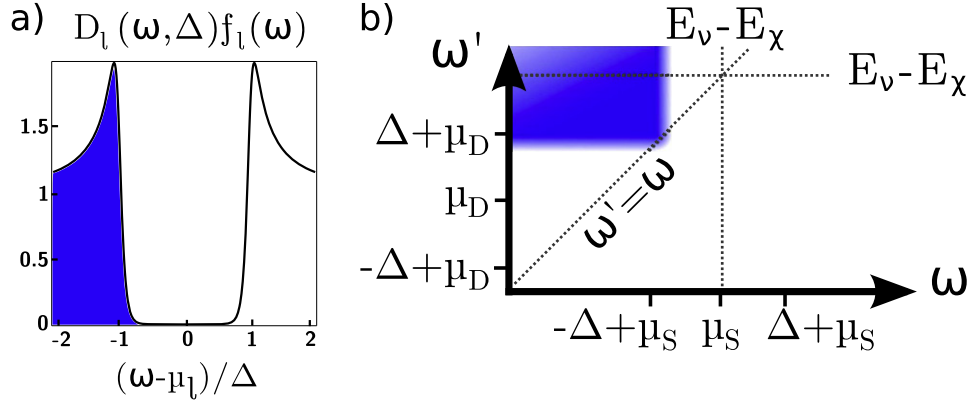


Figure E2. (a) Product of the Fermi function and the BCS density of states for low temperatures. (b) Integrand $I(\omega, \omega')$ occurring in the two-dimensional integral of equation (E.1). The three dashed lines correspond to the roots of the denominator of $I(\omega, \omega')$. The figure shows the parameter regime at low temperatures $T \ll \Delta/k_B$ and finite bias $V_{SD} = (\mu_S - \mu_D)/e > 0$ at which the onset of elastic cotunneling occurs. When the bias voltage is set such that $-\Delta + \mu_S = \Delta + \mu_D$, the corner of the blue region meets the root line $\omega = \omega'$, as shown in the figure, yielding the threshold for elastic cotunneling.

the corner of the blue region, as seen in figure E2(b), where the product of density of state and the Fermi function has its largest value, resulting in a peak structure in the voltage characteristics.

For higher temperatures additional scenarios have to be taken into account because the orange regions in figure E3(b) can no longer be neglected. Thus the condition for a strong Coulomb blockade has to be adapted to the low-bias regime, meaning $\mu_{S/D} + \Delta \ll E_{N\pm 1} - E_N$, to prevent thermally excited sequential tunneling as shown in [18]. For our case this yields $\mu_{S/D} + \Delta \ll E_\nu - E_\chi$. To see a rising of thermal elastic cotunneling, the diagonal $\omega = \omega'$ root has to meet the orange region. Then one has to investigate the cases when the orange regions include the horizontal and the diagonal zeros of the denominators. In this situation we need only a minimal bias $|V_{SD}| \geq 0$. Thus, for large enough temperatures a remarkable contribution of the component of the kernel \hat{K}_{EC} for elastic cotunneling is always present in the bias-gate voltage range since the onset occurs at zero bias, as one can see by means of the condition $-\Delta + \mu_D = \omega' = \omega = -\Delta + \mu_S$.

After analyzing the property of the integrand of the kernel element we can give a first approximation for the elastic cotunneling rate in the middle of a Coulomb diamond for the process shown in figure E1(a). As already explained we have to investigate only the integrand in the energy area, where $\omega \approx \omega'$. Furthermore we investigate the Coulomb diamond ③, in particular, as in the main text, where the center is placed at a gate voltage $V_{\text{gate}} = (\frac{5}{2}E_C + \frac{1}{2}\delta)/e$. Then the energy difference $E_\nu - E_\chi = E_4 - E_3^0 = U/2$, with the ground-state energy being E_3^0 for the three-particle state and E_4 for the four-particle state. Thus in the energy region where the product of the Fermi functions $f_S(\omega)[1 - f_D(\omega)]$ is non-zero the denominator is almost constant, with magnitudes $\pm U/2$. This leads to the result

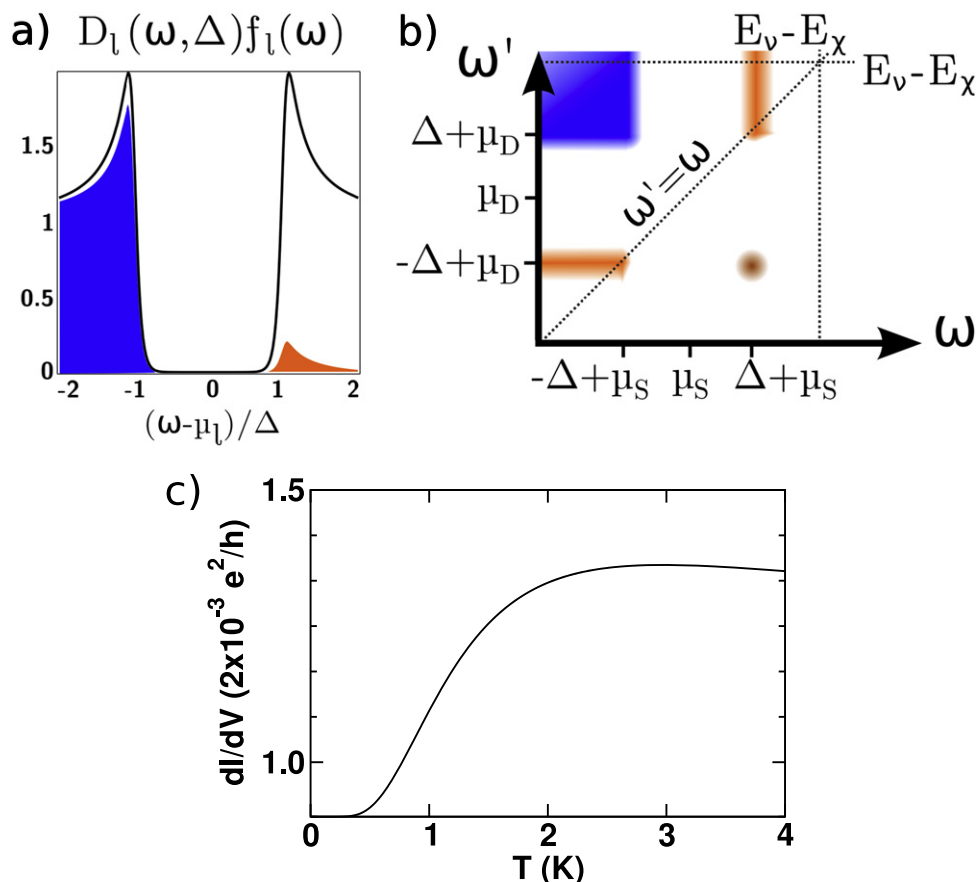


Figure E3. (a) Product of the Fermi function and the BCS density of states for high temperatures. (b) The figure shows the parameter regime at high temperatures $T \lesssim \Delta/k_B$ and $V_{SD} = 0$ at which thermally assisted elastic cotunneling occurs. When the root line $\omega = \omega'$ hits the corners of the orange area, it holds $-\Delta + \mu_S = -\Delta + \mu_D$, corresponding to zero bias. Thus, even in the zero-bias regime, thermally excited elastic cotunneling features emerge which are absent for low temperatures. The dark orange color is important only for high temperatures $T \gtrsim \Delta/k_B$. (c) Temperature dependence of the appearing zero-bias peak in the stability diagram. For comparison we add a conductance offset of about $0.002 e^2/h$ to our numerical data. For small temperatures $T \ll \Delta/k_B$ a Boltzmann-like behavior $\exp[-\Delta/(k_B T)]$ can be identified.

$$\begin{aligned}
 \Gamma_{\text{EC}}^3 \rightarrow 3 &\approx -\hbar \int \frac{d\omega}{2\pi} D_S(\omega, \Delta) D_D(\omega, \Delta) \frac{\Gamma_S \Gamma_D f_S(\omega) (1 - f_D(\omega))}{(-\omega + E_4 - E_3^0)(\omega + E_3^0 - E_4)} \\
 &\approx \hbar \left(\frac{2}{U} \right)^2 \Gamma_S \Gamma_D \int \frac{d\omega}{2\pi} D_S(\omega, \Delta) D_D(\omega, \Delta) f_S(\omega) [1 - f_D(\omega)]. \quad (\text{E.2})
 \end{aligned}$$

In a last step one can transform the parameter ω to obtain the bias voltage $V_{SD} = (\mu_S - \mu_D)/e$ as in equation (9). The result of a calculation of the linear cotunneling conductance in terms of the foregoing rate expression at zero bias is shown in figure E3(c).

Other diagrams contribute to elastic cotunneling. However, using the diagrammatic rules to evaluate their analytic expression, one realizes that they contain two different intermediate

states, with one unit of charge more and one unit less than the state $|\chi\rangle$; hence the two zeros of the corresponding denominator in the integrand are energetically far away from each other, resulting in a smaller contribution to the integral.

We also want to mention the dark orange dot in figure E3(b). In that region the kernel component \hat{K}_{EC} contributes at high temperatures only. This can be explained for the case where the diagonal zeros hit the area, resulting in a condition $-\Delta + \mu_D = \omega' = \omega = \Delta + \mu_S$ for the bias threshold $V_{SD} = -2\Delta/e$. The conductance peak in this bias region corresponds to an onset of a resonant charge current based on thermally excited quasiparticles in the drain producing unoccupied states in the low-energy branch of the BCS density of states even for high temperatures.

Appendix F. Inelastic cotunneling contributions

In the same manner as in the preceding section, we can investigate leading contributions to inelastic cotunneling. To this end we identify the diagram shown in figure E1(b) as a relevant inelastic cotunneling contribution to the kernel component $(\hat{K}_{IC})_{\chi\chi'}^{\chi\chi}$. Here the final state χ' has the same charge state as the initial state χ but is energetically excited compared with the initial state. To obtain the analytic expression of the diagram, we can follow the same prescription as in appendix E or simply use the diagrammatic rules derived in [42]. Thus we obtain

$$\begin{aligned}
(\hat{K}_{IC})_{\chi\chi'}^{\chi\chi} &\equiv \sum_{\vec{k}\sigma, \vec{k}'\sigma'} \sum_{mm'\nu} \int_0^\infty dt' e^{-0^+t'} \int_0^{t'} dt_1' \int_0^{t_1'} dt_2' \\
&\times \left\langle \hat{c}_{S\vec{k}\sigma}^\dagger(\tau) \hat{c}_{S\vec{k}\sigma}(t_2) \right\rangle \left\langle \hat{c}_{D\vec{k}'\sigma'}(t_1) \hat{c}_{D\vec{k}'\sigma'}^\dagger(t) \right\rangle \frac{|T_S|^2 |T_D|^2}{\hbar^4} \\
&\times \left\langle \chi' \left| \hat{d}_{m'\sigma'}(t) \right| \nu \right\rangle \left\langle \nu \left| \hat{d}_{m\sigma}(t_2) \right| \chi \right\rangle \left\langle \chi \left| \hat{d}_{m\sigma}(\tau) \right| \nu \right\rangle \left\langle \nu \left| \hat{d}_{m'\sigma'}(t_1) \right| \chi' \right\rangle \\
&= -i\hbar\Gamma_S\Gamma_D \sum_\nu \int \frac{d\omega}{2\pi} \frac{d\omega'}{2\pi} D_S(\omega, \Delta) D_D(\omega', \Delta) \\
&\times \frac{f_S(\omega)(1 - f_D(\omega'))}{(-\omega + E_\nu - E_\chi + i0^+)(\omega' - \omega + E_{\chi'} - E_\chi + i0^+)} \\
&\times \frac{1}{\omega' + E_{\chi'} - E_\nu + i0^+}. \tag{F.1}
\end{aligned}$$

The analysis of the kernel component and its remarkable contributions is done in the same way as depicted before for the elastic cotunneling case. Again we first focus on the low-temperature regime and derive the condition for the standard inelastic cotunneling events in the Coulomb blockade region. We consider only the case in which the diagonal zeros of the denominator touch the corner of the blue region in figure E2(b). In that case the condition for the bias threshold results in $\Delta + \mu_D = \omega' = \omega + E_\chi - E_{\chi'} = -\Delta + \mu_S + E_\chi - E_{\chi'}$. If we further use the energy difference $E_{\chi'} - E_\chi = \delta$ between the states of the CNT, we obtain the onset of the inelastic cotunneling peak in the current-voltage characteristics at bias voltage $|V_{SD}| = (2\Delta + \delta)/e$. For higher temperatures an additional situation has to be considered. For thermally excited transport features we investigate the case when the diagonal zeros hit the

orange regions in figure E3(b). Here we can give an additional requirement, $-\Delta + \mu_D = \omega' = \omega + E_\chi - E_{\chi'} = -\Delta + \mu_S + E_\chi - E_{\chi'}$, resulting in an onset of a thermal-dependent peak in the conductance measurements at bias voltage $|V_{SD}| = \delta/e$. The peak height of the thermal replica of the standard inelastic cotunneling grows with increasing temperature as more quasiparticles occupy the excited states and thus can contribute to the corresponding transport processes.

A quantitative approximation for the inelastic cotunneling rates in the middle of the Coulomb diamond for the process shown in figure E1(b) can now be obtained when we investigate the integrand in the energy region $\omega' \approx \omega - \delta$. In the same manner as before we can then write the rate in Coulomb diamond ③ as

$$\begin{aligned} \Gamma_{\text{EC}}^{3 \rightarrow 3^*} &\approx -\hbar \int \frac{d\omega}{2\pi} D_S(\omega, \Delta) D_D(\omega - \delta, \Delta) \\ &\quad \times \frac{\Gamma_S \Gamma_D f_S(\omega) (1 - f_D(\omega - \delta))}{(-\omega + E_4 - E_3^0)(\omega - \delta + E_3^* - E_4)} \\ &\approx \hbar \left(\frac{2}{U}\right)^2 \Gamma_S \Gamma_D \int \frac{d\omega}{2\pi} D_S(\omega, \Delta) D_D(\omega - \delta, \Delta) f_S(\omega) [1 - f_D(\omega - \delta)], \end{aligned} \quad (\text{F.2})$$

where the three-particle energy E_3^* of the excited state was used.

References

- [1] Glazman L I and Matveev K A 1989 *JETP Lett.* **49** 659
- [2] Baselmans J, Morpurgo A F, van Wees B and Klapwijk T M 1999 *Nature* **397** 43
- [3] Rozhkov A V, Arovas D P and Guinea F 2001 *Phys. Rev. B* **64** 233301
- [4] Doh Y J, van Dam J A, Roest A L, Bakkers E P A M, Kouwenhoven L P and De Franceschi S 2005 *Science* **309** 272
- [5] van Dam J A, Nazarov Y V, Bakkers E, De Franceschi S and Kouwenhoven L 2006 *Nature* **442** 667
- [6] Jarillo-Herrero P, van Dam J A and Kouwenhoven L 2006 *Nature* **439** 953
- [7] Scheer E, Belzig W, Naveh Y, Devoret M H, Esteve D and Urbina C 2001 *Phys. Rev. Lett.* **86** 284
- [8] Buitelaar M R, Belzig W, Nussbaumer T, Babić B, Bruder C and Schönberger C 2003 *Phys. Rev. Lett.* **91** 057005
- [9] Andersen B M, Flensberg K, Koerting V and Paaske J 2011 *Phys. Rev. Lett.* **107** 256802
- [10] Deon F, Pellegrini V, Giazotto F, Biasiol G, Sorba L and Beltram F 2011 *Phys. Rev. B* **84** 100506
- [11] Yeyati A L, Cuevas J C, López-Dávalos A and Martín-Rodero A 1997 *Phys. Rev. B* **55** 6137
- [12] Golovach V N and Loss D 2004 *Phys. Rev. B* **69** 245327
- [13] Eichler A, Weiss M, Oberholzer S, Schönberger C, Levy Yeyati A, Cuevas J C and Martín-Rodero A 2007 *Phys. Rev. Lett.* **99** 126602
- [14] Grove-Rasmussen K, Jørgensen H I, Andersen B M, Paaske J, Jespersen T S, Nygård J, Flensberg K and Lindelof P E 2009 *Phys. Rev. B* **79** 134518
- [15] Dirks T, Chen Y F, Birge N O and Mason N 2009 *Appl. Phys. Lett.* **95** 192103
- [16] De Franceschi S, Kouwenhoven L, Schönberger C and Wernsdorfer W 2010 *Nat. Nanotechnol.* **5** 703
- [17] Pfaller S, Donarini A and Grifoni M 2013 *Phys. Rev. B* **87** 155439
- [18] Gaass M, Pfaller S, Geiger T, Donarini A, Grifoni M, Hüttel A K and Strunk C 2014 *Phys. Rev. B* **89** 241405
- [19] Johansson G, Bratus E N, Shumeiko V S and Wendin G 1999 *Phys. Rev. B* **60** 1382
- [20] Günel H Y, Batov I E, Hardtdegen H, Sladek K, Winden A, Weis K, Panaitov G, Grützmacher D and Schäpers T 2012 *J. Appl. Phys.* **112** 034316

- [21] Averin D V and Nazarov Y V 1990 *Phys. Rev. Lett.* **65** 2446
- [22] Kong J, Soh H, Cassell A, Quate C and Dai H 1998 *Nature* **395** 878
- [23] Pallecchi E, Gaaß M, Ryndyk D A and Strunk C 2008 *Appl. Phys. Lett.* **93** 072501
- [24] Martinis J M and Kautz R L 1989 *Phys. Rev. Lett.* **63** 1507
- [25] Hulm J, Jones C, Hein R and Gibson J 1972 *J. Low Temp. Phys.* **7** 291
- [26] Mayadas A F, Laibowitz R B and Cuomo J J 1972 *J. Appl. Phys.* **43** 1287
- [27] Kumar A, Gaim M, Steininger D, Yeyati A L, Martín-Rodero A, Hüttel A K and Strunk C 2014 *Phys. Rev. B* **89** 075428
- [28] Buitelaar M R, Nussbaumer T and Schönenberger C 2002 *Phys. Rev. Lett.* **89** 256801
- [29] Siano F and Egger R 2004 *Phys. Rev. Lett.* **93** 047002
- [30] Cleuziou J P, Wernsdorfer W, Bouchiat V, Ondarcuhu T and Monthieux M 2006 *Nat. Nanotechnol.* **1** 53
- [31] Kim B K, Ahn Y H, Kim J J, Choi M S, Bae M H, Kang K, Lim J S, López R and Kim N 2013 *Phys. Rev. Lett.* **110** 076803
- [32] Lee Eduardo J H, Jiang X, Houzet M, Aguado R, Lieber C M and De Franceschi S 2014 *Nat. Nanotechnol.* **9** 79
- [33] Chang W, Manucharyan V E, Jespersen T S, Nygård J and Marcus C M 2013 *Phys. Rev. Lett.* **110** 217005
- [34] Laird E A, Kuemmeth F, Steele G, Grove-Rasmussen K, Nygård J, Flensberg K and Kouwenhoven L P 2014 arxiv:1403.6113
- [35] Bogoljubov N 1958 *Il Nuovo Cimento* **7** 794
- [36] Valatin J 1958 *Il Nuovo Cimento* **7** 843
- [37] Josephson B 1962 *Phys. Lett.* **1** 251
- [38] Bardeen J 1962 *Phys. Rev. Lett.* **9** 147–9
- [39] Blum K 2012 *Density Matrix Theory and Applications (Springer Series on Atomic)* (Berlin: Springer)
- [40] Weymann I, König J, Martinek J, Barnaś J and Schön G 2005 *Phys. Rev. B* **72** 115334
- [41] Koller S, Grifoni M, Leijnse M and Wegewijs M R 2010 *Phys. Rev. B* **82** 235307
- [42] Governale M, Pala M G and Knig J 2008 *Phys. Rev. B* **77** 134513
- [43] Dynes R C, Narayanamurti V and Garno J P 1978 *Phys. Rev. Lett.* **41** 1509
- [44] Jespersen T S, Grove-Rasmussen K, Paaske J, Muraki K, Fujisawa T, Nygard J and Flensberg K 2011 *Nat. Phys.* **7** 348
- [45] Pecker S, Kuemmeth F, Secchi A, Rontani M, Ralph D C, McEuen P L and Ilani S 2013 *Nat. Phys.* **9** 576
- [46] Schleser R, Ihn T, Ruh E, Ensslin K, Tews M, Pfannkuche D, Driscoll D C and Gossard A C 2005 *Phys. Rev. Lett.* **94** 206805
- [47] Hüttel A K, Witkamp B, Leijnse M, Wegewijs M R and van der Zant H S J 2009 *Phys. Rev. Lett.* **102** 225501
- [48] Anderson P W and Rowell J M 1963 *Phys. Rev. Lett.* **10** 230
- [49] Josephson B D 1974 *Rev. Mod. Phys.* **46** 251
- [50] Bardeen J, Cooper L N and Schrieffer J R 1957 *Phys. Rev.* **108** 1175
- [51] Schrieffer J 1999 *Theory of Superconductivity (Advanced Book Program Series)* (New York: Perseus)